Global-Local model for guided wave scattering problems with application to defect characterization in built-up composite structures.

Antonino Spada[a], Margherita Capriotti[b], Francesco Lanza di Scalea[b]

[a]Department of Civil, Environmental, Aerospace, Materials Engineering (DICAM), University of Palermo, Viale delle Scienze, Ed. 8, 90128 Palermo (PA), Italy; antonino.spada@unipa.it
[b]NDE&SHM Laboratory, Department of Structural Engineering, University of California San Diego, 9500 Gilman Drive, La Jolla, CA 92093-0085, USA;
mcapriot@eng.ucsd.edu, flanzadiscalea@ucsd.edu

Declarations of Interest: none.

Corresponding author: Francesco Lanza di Scalea, Department of Structural Engineering, University of California San Diego, 9500 Gilman Drive, La Jolla, CA 92093-0085, USA;
Tel: +1-858-8221458, Email: flanzadiscalea@ucsd.edu

Abstract

Predicting scattering in waveguide solids with geometrical and/or material discontinuities is of great interest to many fields, including ultrasonic-based Non-Destructive Testing (NDT) and Structural Health Monitoring (SHM) of structural components. The problem is complicated by the multimode and dispersive behaviour of the guided waves. This paper describes a unified Global-Local (GL) approach that is computationally efficient in cases that can be very complex in terms of geometry and/or material properties and for which wave theoretical solutions are impractical or non-existent. One example of this is a composite built-up structure. The proposed GL procedure discretizes the "local" region with the scattering discontinuity by regular finite elements, and utilizes the efficient Semi-Analytical Finite Element solutions in the "global" region away from the scatterer. A unified formulation is presented for this approach, including the dispersive unforced solutions for each applicable mode, the mode tracking, the scattering spectra (reflection and transmission), and the energy balance calculations. The algorithm is applied to the case of a composite skin-to-stringer assembly used in modern aircraft construction. Various representative defects in this assembly are modelled, and transmission spectra are calculated for either axial or flexural guided wave modes used in excitation. These scattering spectra reveal interesting behaviours that are peculiar to each of the defects. The predictions can be extremely useful to design a guided-wave NDE or SHM test aimed at optimally detecting a specific defect and/or at identifying the type of defect being detected.

KEYWORDS: *Guided elastic waves, scattering, global-local method, semi-analytical finite element method, composite structures, non-destructive testing, structural health monitoring*

1. Introduction

"Guided" elastic waves are widely used to probe structural components with waveguide geometries (plates, rod, pipes, etc..) in Non-Destructive Testing (NDT) and Structural Health Monitoring (SHM) applications. Lamb waves, for example, are specific guided waves in traction-free isotropic plates. Guided waves can maximize the inspection range by exploiting the long propagation distances, while maintaining a sufficient sensitivity to small structural anomalies (e.g. defects) owing to the relatively large frequencies (~ 100's kHz for typical plate-like structures). However, the propagation of guided waves is complicated by their multimode character (several wave modes propagating simultaneously) and dispersive character (propagation velocity is a function of frequency). Additional complications exist in the case of anisotropic layered components (e.g. laminated composites) and/or built-up structures (e.g. stiffened panels) where the guided wave crosses elements of varying thickness along its path.

The vast majority of the structure of modern military and commercial aircrafts (e.g. B787, A380) is made of fiber-reinforced composite materials, owing to their high strength-to-weight and stiffness-to-weight ratios. The complexities of the manufacturing process as well as the severity of external loads in flight can develop a number of structural defects that need to be detected and quantified through NDT or SHM techniques. Ultrasonic guided waves are an ideal candidate for this task (Staszewsky et al., 2004).

Predicting the scattering behaviour of ultrasonic waves in the presence of specific structural defects is essential to (a) properly guide the experimental implementation of an NDT/SHM test through proper selection of mode-frequency combinations, and (b) provide quantitative, rather than qualitative information on a defect from knowledge of the given defect's scattering pattern. Such wave propagation predictions are very challenging in fuselage and wing aircraft components that are anisotropic, multi-layered, and stiffened by built-up stringers.

Analytical solutions of guided wave propagation through multi-layered structures exist using well known global matrix or transfer matrix methods (Rose, 2014). However, purely theoretical predictions become quite challenging, or non-existent, in the presence of structural discontinuities such as defects. Datta et al. (1988) used an approximated stiffness method to study guided dispersive propagation in laminated anisotropic plates. Castaings et al. (2002) applied the modal decomposition method to analyze scattering of an incident symmetric (axial) S0 or anti-symmetric (flexural) A0 Lamb mode by an internal or an opening crack in isotropic plates, imposing velocity and stress continuity conditions at the crack section. An improved analytical approach to predict Lamb waves scattering from a step geometrical discontinuity considering a complex mode expansion with vector projection was recently proposed by Giurgiutiu and co-workers (Podder and Giurgiutiu, 2016a, 2016b; Haider et al., 2018). These studies apply to isotropic plates with thickness changes, presence of stiffeners, and horizontal cracks or disbonds. These problems can be modelled by adjacent sub-regions with rectangular geometry (sub-plates).

Numerical methods can provide more flexibility to handle more complicated geometries and defects. Guo and Cawley (1993), for example, applied the Finite Element (FE) method to investigate the interaction of the S0 Lamb mode with delaminations at different interfaces in a composite laminate. However, in order to maximize computational efficiency and maintaining accuracy at small wavelengths, it is often not optimum to carry out an FE analysis for the entire domain. When the structural details and anomalies are only a localized region of the entire "waveguide" panel, a hybrid Global-Local approach is more appropriate. Hybrid methods couple the solution available analytically in the "global" region with that available numerically (BEM or FEM) in the "local" region with the structural discontinuity. The general hybrid method to predict elastic wave scattering based on a FE discretization of the local region was utilized for axisymmetric inclusions in homogeneous isotropic media (Goetschel et al., 1982), other axially-symmetric scattering problems (Rattanawangcharoen et al., 1997), isotropic plates with notches and rivet-hole cracks (Chang and Mal, 1999; Mal and Chang, 2000; Zhou and Ichchou, 2011), defects in lap-shear joints of isotropic plates (Chang and Mal, 1995), and isotropic plates with a normal transversely isotropic weld (Al-Nassar et al., 1991). The problem of reflections of a fixed cracked edge was addressed by Karunasena et al. (1995), while the scattering from a semi-infinite plate employing the BEM method for the local part was studied by Galan and Abascal (2002), who later extended their BE-FE technique to plates with inclusions, different cracks and materials (Galan and Abascal, 2005).

Other works focused on wave scattering in composite plates. The use of a hybrid FE local discretization coupled with a boundary integral representation of the global part was investigated by Datta et al. (1992) for the case of a uniaxial composite plate. Boundary integral formulations were utilized to study scattering from interface cracks in a layered half-space and layered fiber—reinforced composites (Karim and Kundu, 1988; Karim et al., 1989; Karim et al., 1992). FE local-global techniques were applied to scattering in layered composite laminates with delaminations (Tian et al., 2004) and free edges (Dong and Goetschel, 1982).

The vast majority of these previous works utilized theoretical solutions (mostly normal mode expansion) to model the guided wave propagation in the global portion of the isotropic or composite plate. However, such theoretical guided wave solutions are increasingly difficult to obtain for an anisotropic composite laminate with a general number of layers. For this reason some of the authors of the present paper have recently exploited the numerical efficiency of the Semi-Analytical Finite Element method (SAFE) (Hayashi et al., 2003; Bartoli et al. 2006; Marzani et al., 2008) to deal with the global portion of the GL scattering problem in composite plates of arbitrary number of layers with delamination defects (Srivastava and Lanza di Scalea, 2010). A similar use of SAFE in Global-Local scattering problems for layered composites was shown later by Ahmad et al. (2013). The SAFE method only requires the FE discretization of the cross-section of the laminate composite, and utilizes basic theoretical harmonic wave solutions in the wave propagation direction. SAFE easily deals with the particular composite lay-up by simply rotating the stiffness matrix of each layer in the wave propagation direction. In a Global-Local framework, the SAFE global solutions are matched to the FE local solutions through continuity of displacements and tractions at the local-global boundaries, as customary of hybrid approaches.

The present paper builds on the work by Srivastava and Lanza di Scalea (2010) to unify the global (SAFE) -local (FE) formulation and implement it in a computationally efficient code able to solve extremely complex scattering problems such as layered composite laminates with built-up geometries. The method is applied to studying guided wave scattering in a composite skin-to-stringer assembly that is widely used in modern aircraft construction. The Global-Local method formulated here allows to efficiently predict reflection and transmission spectra of the relevant guided wave modes that can be utilized for an optimized NDE or SHM test of the structure. Despite the criticality of skin-to-stinger assemblies in aircraft and the consequent high need for inspections

(Capriotti et al., 2017), the authors are not aware of any previous quantitative study aimed at predicting wave scattering from defects in these components. The reason is the material and geometrical complexity of this assembly, that instead presents a great opportunity for the proposed Global-Local formulation.

2. The Unified Global-Local method

2.1 Problem statement

Let us consider the general scattering case shown in Fig. 1. An incident time harmonic guided wave travelling along the *x* positive direction in a prismatic region (global region) is scattered into reflected and transmitted waves after interacting with a (local) region with geometrical discontinuities (e.g. build-ups) and/or structural defects (e.g. cracks, delaminations, etc..).

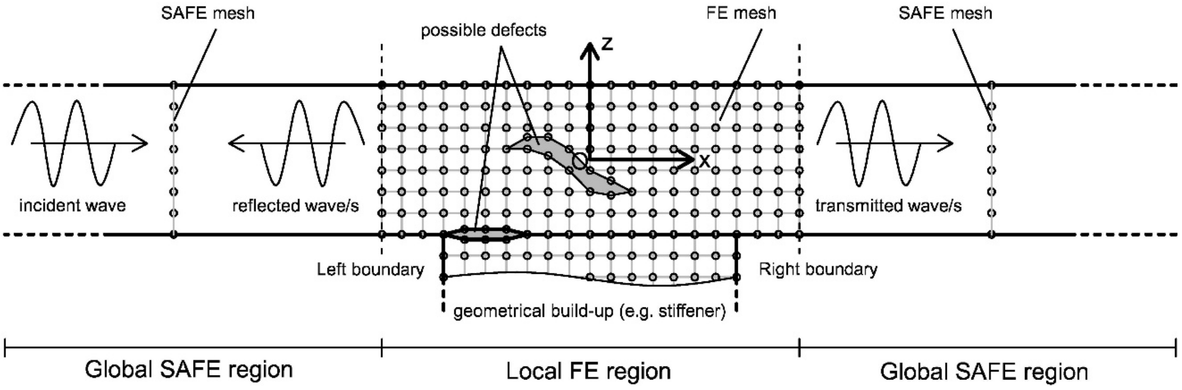

Fig. 1. Geometrical representation of the scattering of an incident wave in a waveguide prismatic structure in reflected and transmitted waves from a local region with geometrical and/or material discontinuities.

The equilibrium of each part of the problem is guaranteed by the Principle of Virtual Work (PVW). The general weak form for the harmonic elasto-dynamic case, written considering virtual displacements and strains, is (in Voigt's notation):

$$\int_{\Omega} \delta\bar{\boldsymbol{\varepsilon}}^T \boldsymbol{\sigma}\, d\Omega = \int_{\Gamma_t} \delta\bar{\mathbf{u}}^T \mathbf{t}\, d\Gamma - \int_{\Omega} \delta\bar{\mathbf{u}}^T \left(\rho \ddot{\mathbf{u}}\right) d\Omega \tag{1}$$

where $\mathbf{u} = \begin{bmatrix} u_x & u_y & u_z \end{bmatrix}^T$, $\mathbf{t} = \begin{bmatrix} t_x & t_y & t_z \end{bmatrix}^T$, $\boldsymbol{\varepsilon} = \begin{bmatrix} \varepsilon_x & \varepsilon_y & \varepsilon_z & \gamma_{yz} & \gamma_{xz} & \gamma_{xy} \end{bmatrix}^T$, and $\boldsymbol{\sigma} = \begin{bmatrix} \sigma_x & \sigma_y & \sigma_z & \tau_{yz} & \tau_{xz} & \tau_{xy} \end{bmatrix}^T$ are displacement, traction, strain and stress vectors respectively. All these variables are space and time dependent. In Eq. (1) the bar above a letter stands for complex conjugate, while $\ddot{\mathbf{u}}$ is the acceleration, ρ the density, Ω the volume of the medium and Γ_t the medium's loaded external surface. In this work, body forces and damping effects are neglected.

In order to model both reflections and transmissions, the entire domain Ω is subdivided into one "local" region in the center and two "global" regions on either side. Fig. 1 shows a plain strain case (that is assumed in the application problem studied in this paper), where the cross-sectional SAFE discretization of the global waveguide reduces to a 1D mesh along z, and a full FE mesh is instead used in 2D domain (x-z plane) for the local region. The extension of the concept to a general 3D case is trivial (2D SAFE discretization in the global region and 3D FE discretization in the local region). The GL formulation as written here applies to a general 3D case.

2.2 *Local and global weak form solutions*

Let us imagine separating the local region from the global region at their left and right boundaries of Fig. 1. Since equilibrium must continue to hold, internal tractions arise at each boundary due to the internal stress caused by the application of external actions. Using the PVW for each region, the traction vector **t** in Eq. (1) consists of the internal tractions at the boundaries, which behave as new external forces. The vector **t** could be evaluated as $\mathbf{t} = \boldsymbol{\sigma}\mathbf{n}$, with **n** the unit vector normal to the Γ_t surface and $\boldsymbol{\sigma}$ the stress second-order tensor. Alternatively, using Voigt notation:

$$\mathbf{t} = \mathbf{L}_n^T \boldsymbol{\sigma} \tag{2}$$

where

$$\mathbf{L}_n = \begin{bmatrix} n_x & 0 & 0 \\ 0 & n_y & 0 \\ 0 & 0 & n_z \\ 0 & n_z & n_y \\ n_z & 0 & n_x \\ n_y & n_x & 0 \end{bmatrix} \tag{3}$$

with n_x, n_y, n_z the direction cosines of the normal **n**. In what follows, a superscript 'ℓ' or 'g' is adopted to identify quantities referring to the "local" region or the "global" region, respectively.

The local region is discretized by 2D or 3D finite elements. Accordingly, the approximate displacement $\mathbf{u}_h^{\ell-e}$ at a point inside the local e-th element is obtained from the nodal values $\mathbf{d}^{\ell-e}$ through the shape functions $\mathbf{N}^{\ell}$ using known FE concepts:

$$\mathbf{u}_h^{\ell-e}(x,y,z,t) = \mathbf{N}^{\ell}(x,y,z)\,\mathbf{d}^{\ell-e}\,e^{-i\omega t} \tag{4}$$

where ω is the circular frequency.
The corresponding approximate strains and stresses are

$$\boldsymbol{\varepsilon}_h^{\ell-e} = \mathbf{L}\,\mathbf{u}_h^{\ell-e} \tag{5}$$

$$\boldsymbol{\sigma}_h^{\ell-e} = \mathbf{C}^{\ell-e}\,\boldsymbol{\varepsilon}_h^{\ell-e} \tag{6}$$

where $\mathbf{L}$ and $\mathbf{C}^{\ell-e}$ are the compatibility and constitutive matrices respectively, with $\mathbf{C}^{\ell-e}$ a real matrix for purely elastic cases, and a complex matrix for viscoelastic cases.

Including all the approximate variables in Eq. (1) and defining the vector $\mathbf{U}^{\ell}$ for the entire nodal local displacements, the dynamic undamped equilibrium equations for the local region are obtained as:

$$\left(\mathbf{K}^{\ell}-\omega^{2}\mathbf{M}^{\ell}\right)\mathbf{U}^{\ell}=\mathbf{F}^{\ell}, \tag{7}$$

with $\mathbf{K}^{\ell}$, $\mathbf{M}^{\ell}$ and $\mathbf{F}^{\ell}$ the classic FE stiffness matrix, mass matrix and force vector.
To interpolate the displacements of the global region, the same procedure is followed, but in a simplified manner. The SAFE method adopts a harmonic exponential term, $e^{i(\xi x-\omega t)}$, to describe analytically the wave behaviour in the wave propagation direction, *x*, where ξ represents the wave number. By combining the analytical solution along the wave propagation with an FE cross-sectional (*y*-*z*) discretization, the approximate displacement $\mathbf{u}_h^{g-e}$ within a single SAFE element of the global region can be written as:

$$\mathbf{u}_h^{g-e}\left(x,y,z,t\right)=\mathbf{N}^{g}\left(y,z\right)\,\mathbf{d}^{g-e}\,e^{i(\xi x-\omega t)} \tag{8}$$

with $\mathbf{d}^{g-e}$ the nodal displacements and $\mathbf{N}^{g}$ the shape functions of the global cross-sectional mesh. Following the same steps discussed in Bartoli et al. (2006) or in Rose (2014), the expression of the approximate strain vector in SAFE is derived as:

$$\boldsymbol{\varepsilon}_h^{g-e}=\left(\mathbf{B}_1+i\xi\mathbf{B}_2\right)\mathbf{d}^{g-e}e^{i(\xi x-\omega t)} \tag{9}$$

where

$$\mathbf{B}_1=\mathbf{L}_y\mathbf{N}^{g}_{,y}+\mathbf{L}_z\mathbf{N}^{g}_{,z}\qquad\text{and}\qquad\mathbf{B}_2=\mathbf{L}_x\mathbf{N}^{g} \tag{10}$$

are two compatibility matrices.
In Eq. (10) $\mathbf{L}_x$, $\mathbf{L}_y$ and $\mathbf{L}_z$ are particularized expressions of $\mathbf{L}_n$ given in Eq. (3) for a unit normal vector aligned to the *x*, *y* or *z* axis respectively, while $\mathbf{N}^{g}_{,y}$ and $\mathbf{N}^{g}_{,z}$ are the derivatives of the global shape function matrix with respect to the *y* or *z* coordinates. Approximate strains are then transformed into approximate stresses by applying the constitutive laws

$$\boldsymbol{\sigma}_h^{g-e}=\mathbf{C}^{g-e}\,\boldsymbol{\varepsilon}_h^{g-e} \tag{11}$$

with $\mathbf{C}^{g-e}$ the element constitutive matrix for the global region.

It is worth noting that in Eqs. (6) and (11) the constitutive matrices must refer to the (O, *x*, *y*, *z*) reference system. Therefore, for anisotropic materials, any local stiffness matrix $\tilde{\mathbf{C}}$ (e.g. lamina in the principal directions of material symmetry) needs to be transformed to the general (O, *x*, *y*, *z*) system **C** according to

$$\mathbf{C}=\mathbf{R}^{T}\tilde{\mathbf{C}}\,\mathbf{R} \tag{12}$$

with **R** the transformation matrix.

For the particular case of a laminated composite whose lamina is oriented at an angle ϑ with respect to the x direction, the transformation matrix is:

$$\mathbf{R}=\begin{bmatrix} m^2 & n^2 & 0 & 0 & 0 & mn \\ n^2 & m^2 & 0 & 0 & 0 & -mn \\ 0 & 0 & 1 & 0 & 0 & 0 \\ 0 & 0 & 0 & m & -n & 0 \\ 0 & 0 & 0 & n & m & 0 \\ -2mn & 2mn & 0 & 0 & 0 & m^2-n^2 \end{bmatrix} \tag{13}$$

with $m=\cos\vartheta$ and $n=\sin\vartheta$.
With Eqs. (8)-(11) and (2) at hand, the PVW applied to the semi-infinite global region gives:

$$\left(\mathbf{K}^{\mathrm{g}}-\omega^2\mathbf{M}^{\mathrm{g}}\right)\mathbf{U}^{\mathrm{g}}=\mathbf{F}^{\mathrm{g}} \tag{14}$$

where $\mathbf{U}^{\mathrm{g}}$ is the vector collecting the displacements of all the nodes of the global region mesh. Furthermore:

$$\mathbf{K}^{\mathrm{g}}=\underset{e=1}{\overset{n_{el}}{\mathrm{A}}}\int\limits_{\Omega^{\mathrm{g}-e}}\left(\mathbf{B}_1-i\xi\mathbf{B}_2\right)^T\mathbf{C}^{\mathrm{g}-e}\left(\mathbf{B}_1+i\xi\mathbf{B}_2\right)d\Omega \tag{15}$$

$$\mathbf{M}^{\mathrm{g}}=\underset{e=1}{\overset{n_{el}}{\mathrm{A}}}\int\limits_{\Omega^{\mathrm{g}-e}}\left(\mathbf{N}^{\mathrm{g}}\right)^T\rho^e\,\mathbf{N}^{\mathrm{g}}\,d\Omega \tag{16}$$

$$\mathbf{F}^{\mathrm{g}}=\left[\underset{e=1}{\overset{n_{el}}{\mathrm{A}}}\int\limits_{\Gamma_t^{\mathrm{g}-e}}\left(\mathbf{N}^{\mathrm{g}}\right)^T\mathbf{L}_n^T\,\mathbf{C}^{\mathrm{g}-e}\left(\mathbf{B}_1+i\xi\mathbf{B}_2\right)d\Gamma\right]\mathbf{U}^{\mathrm{g}} \tag{17}$$

are the stiffness matrix, mass matrix and force vector, respectively.
In Eqs. (15)-(17) $\underset{e=1}{\overset{n_{el}}{\mathrm{A}}}$ symbolizes the assembly operator, with n_{el} the total number of elements.

2.3 Global-local solution

Referring again to the scattering case of Fig. 1, it can be assumed that the nodal displacements $\mathbf{q}_{lB}$ recorded at the left boundary is a combination of the incident wave and the reflected waves. The nodal displacements $\mathbf{q}_{rB}$ at the right boundary, instead, are those of the transmitted waves. Hence:

$$\begin{gathered}\mathbf{q}_{lB}=\mathbf{q}_{incident}+\mathbf{q}_{reflected}, \\ \mathbf{q}_{rB}=\mathbf{q}_{transmitted}.\end{gathered} \tag{18}$$

In the subject case of multimode guided waves, the incident, reflected and transmitted waves can be thought of as the superimposition of a finite number N_M of global cross-sectional mode shapes, each amplified by a participation coefficient having the physical meaning of the amplitude of the single wave mode.

The incident mode can be modelled by imposed displacements or forces at the source. In the present paper, a pure incident mode is generated by imposing the unique cross-sectional displacement shapes at the relevant frequencies for the chosen mode. The evaluation of the unique mode shapes is performed by solving an eigenproblem, that is shown in the next section. If the symbol $\mathbf{\Phi}$ is used to represent the generic mode shape, and the factor $e^{-i\omega t}$ is omitted for simplicity, Eqs. (18) are explicitly rewritten as:

$$\mathbf{q}_{lB} = \mathbf{\Phi}_{in}^{+}\, e^{i\left[\xi_{in}^{+}\left(d_s - x_{lB}\right)\right]} + \sum_{j=1}^{N_M} A_j^{-}\, \mathbf{\Phi}^{(j)^{-}}\, e^{i\left(-\xi_j^{-}\, x_{lB}\right)} \tag{19}$$

$$\mathbf{q}_{rB} = \sum_{j=1}^{N_M} A_j^{+}\, \mathbf{\Phi}^{(j)^{+}}\, e^{i\left(\xi_j^{+}\, x_{rB}\right)} \tag{20}$$

where the superscript "+" represents a wave travelling in the right and the superscript "-" a wave travelling in the left direction. Therefore: $\mathbf{\Phi}_{in}^{+}$ and ξ_{in}^{+} are mode shape and wavenumber of the incident wave (assumed at unity amplitude); A_j^{-}, $\mathbf{\Phi}^{(j)^{-}}$ and ξ_j^{-} are amplitude, mode shape and wavenumber of the *j*-th reflected mode; and A_j^{+}, $\mathbf{\Phi}^{(j)^{+}}$ and ξ_j^{+} amplitude, mode shape and wavenumber of the *j*-th transmitted mode. d_s, x_{lB} and x_{rB} measure the distances of the source, left boundary and right boundary, respectively, from the origin of the reference system that is set at the center of the local region (see Fig. 1).

Eqs. (19) and (20) can be rewritten in a compact form:

$$\mathbf{q}_{lB} = \mathbf{\Phi}_{in}^{+}\, e^{i\left[\xi_{in}^{+}\left(d_s - x_{lB}\right)\right]} + \mathbf{G}^{-}\, \mathbf{D}^{-} \tag{21}$$

$$\mathbf{q}_{rB} = \mathbf{G}^{+}\, \mathbf{D}^{+} \tag{22}$$

where

$$\mathbf{G}^{\pm} = \begin{bmatrix} \mathbf{\Phi}^{(1)^{\pm}} & \mathbf{\Phi}^{(2)^{\pm}} & \cdots & \mathbf{\Phi}^{(j)^{\pm}} & \cdots & \mathbf{\Phi}^{(N_M)^{\pm}} \end{bmatrix} \tag{23}$$

$$\mathbf{D}^{\pm} = \begin{bmatrix} D_1^{\pm} & D_2^{\pm} & \cdots & D_j^{\pm} & \cdots & D_{N_M}^{\pm} \end{bmatrix}^T, \tag{24}$$

with

$$D_j^{+} = A_j^{+}\, e^{i\left(\xi_j^{+}\, x_{rB}\right)} \tag{25}$$

$$D_j^{-} = A_j^{-}\, e^{i\left(-\xi_j^{-}\, x_{lB}\right)}. \tag{26}$$

Eqs. (21) and (22) are entirely composed of known terms, except for the $A_j^{\pm}$ amplitudes. These equations also guarantee the continuity of displacements between the global and the local regions. The evaluation of $A_j^{\pm}$ is therefore performed in order to also guarantee the continuity of tractions at the left and the right boundaries.

Let us recall the equilibrium Eq. (7) for the local region. A partition of Eq. (7) can be performed in order to separate the contribution of the inner (I) and boundary (B) degrees of freedom, obtaining:

$$\begin{bmatrix} \mathbf{S}_{II} & \mathbf{S}_{IB} \\ \mathbf{S}_{BI} & \mathbf{S}_{BB} \end{bmatrix} \begin{bmatrix} \mathbf{U}_I^{\ell} \\ \mathbf{U}_B^{\ell} \end{bmatrix} = \begin{bmatrix} \mathbf{0} \\ \mathbf{F}_B^{\ell} \end{bmatrix} \tag{27}$$

where

$$\mathbf{S} = \mathbf{K}^{\ell} - \omega^2 \mathbf{M}^{\ell}, \tag{28}$$

$$\mathbf{U}_B^{\ell} = \begin{bmatrix} \mathbf{q}_{lB}^T & \mathbf{q}_{rB}^T \end{bmatrix}^T, \tag{29}$$

$$\mathbf{F}_B^{\ell} = \begin{bmatrix} \left(\mathbf{f}_{lB}^{\ell}\right)^T & \left(\mathbf{f}_{rB}^{\ell}\right)^T \end{bmatrix}^T. \tag{30}$$

In Eq. (30) $\mathbf{f}_{lB}^{\ell}$ and $\mathbf{f}_{rB}^{\ell}$ are the force vectors at the left and right boundaries. They are obtained as the opposites of the consistent nodal force vectors at the same boundaries but considered as belonging to the global regions.

From Eq. (17), for a unit normal vector **n** identifying the positive or negative directions of the *x* axis ($\mathbf{n} = \begin{bmatrix} \pm 1 & 0 \end{bmatrix}^T$), the consistent nodal force vectors for the two global regions are equal to:

$$\mathbf{F}_{lB}^{\mathrm{g}} = \mathbf{F}_{in}^{+} \, e^{i\left[\xi_{in}^{+}\left(d_s - x_{lB}\right)\right]} + \mathbf{F}^{-} \, \mathbf{D}^{-} \tag{31}$$

$$\mathbf{F}_{rB}^{\mathrm{g}} = \mathbf{F}^{+} \, \mathbf{D}^{+} \tag{32}$$

where

$$\mathbf{F}^{\pm} = \begin{bmatrix} \mathbf{F}^{(1)^{\pm}} & \mathbf{F}^{(2)^{\pm}} & \cdots & \mathbf{F}^{(j)^{\pm}} & \cdots & \mathbf{F}^{(N_M)^{\pm}} \end{bmatrix} \tag{33}$$

and

$$\mathbf{F}_{in}^{+} = \left[\mathop{\mathrm{A}}_{e=1}^{n_{el}} \int_{\Gamma_{t_B}^{\mathrm{g}-e}} \left(\mathbf{N}^{\mathrm{g}}\right)^T \mathbf{L}_x^T \, \mathbf{C}^{\mathrm{g}-e} \left(\mathbf{B}_1 + i\,\xi_{in}^{+} \, \mathbf{B}_2\right) d\Gamma \right] \mathbf{\Phi}_{in}^{+}, \tag{34}$$

with

$$\mathbf{F}^{(j)^{\pm}} = \mp \left[\mathop{\mathrm{A}}_{e=1}^{n_{el}} \int_{\Gamma_{t_B}^{\mathrm{g}-e}} \left(\mathbf{N}^{\mathrm{g}}\right)^T \mathbf{L}_x^T \, \mathbf{C}^{\mathrm{g}-e} \left(\mathbf{B}_1 + i\,\xi_j^{\pm} \, \mathbf{B}_2\right) d\Gamma \right] \mathbf{\Phi}^{(j)^{\pm}}. \tag{35}$$

From Eqs. (31) and (32) $\mathbf{f}_{lB}^{\ell}$ and $\mathbf{f}_{rB}^{\ell}$ are obtained as:

$$\mathbf{f}_{lB}^{\ell} = -\mathbf{F}_{lB}^{\mathrm{g}}, \qquad \mathbf{f}_{rB}^{\ell} = -\mathbf{F}_{rB}^{\mathrm{g}}. \tag{36}$$

A static condensation procedure applied to Eq. (27) leads to the following final equations:

$$\left(\mathbf{S}^{*}_{BB}\begin{bmatrix}\mathbf{G}^{-} & \mathbf{0}\\ \mathbf{0} & \mathbf{G}^{+}\end{bmatrix}+\begin{bmatrix}\mathbf{F}^{-} & \mathbf{0}\\ \mathbf{0} & \mathbf{F}^{+}\end{bmatrix}\right)\begin{bmatrix}\mathbf{D}^{-}\\ \mathbf{D}^{+}\end{bmatrix}=-\left(\mathbf{S}^{*}_{BB}\begin{bmatrix}\mathbf{\Phi}^{+}_{in}\\ \mathbf{0}\end{bmatrix}+\begin{bmatrix}\mathbf{F}^{+}_{in}\\ \mathbf{0}\end{bmatrix}\right)e^{i\left[\xi^{+}_{in}\left(d_s-x_{l\mathbf{B}}\right)\right]} \tag{37}$$

where $\mathbf{S}^{*}_{BB}=\mathbf{S}_{BB}-\mathbf{S}_{BI}\,\mathbf{S}^{-1}_{II}\,\mathbf{S}_{IB}$ is the condensed matrix of $\mathbf{S}$.

Eq. (37) is solved to find $\mathbf{D}^{-}$ and $\mathbf{D}^{+}$. Since the coefficient matrix is not square, the least squares method should be applied. Once the $\mathbf{D}^{-}$ and $\mathbf{D}^{+}$ coefficients are known, the unknown A^{-}_{j} and A^{+}_{j} reflected and transmitted amplitudes can be finally determined.

2.4 Dispersion curves and mode shapes evaluation

As seen in the previous section, the GL method exploits the knowledge of at least N_M mode shapes of the guided waves. These are derived as the (unforced) solutions of the equilibrium Eqs. (14) for the global region, which can be particularized as

$$\left[\mathbf{K}_1+i\xi\mathbf{K}_2+\xi^2\mathbf{K}_3-\omega^2\mathbf{M}^{g}\right]_M\mathbf{\Phi}=\mathbf{0} \tag{38}$$

with M the number of total degrees of freedom for the global region mesh.

The stiffness matrices $\mathbf{K}_j\ \left(j=1,2,3\right)$ are derived from Eq. (15) and explicitly given by Bartoli et al. (2006). Eq. (38) constitutes a generalized eigenproblem in ξ and ω. It is a common practice to reduce Eq. (38) to a linear eigenproblem in ξ by doubling the size of the problem:

$$\left[\mathbf{A}-\xi\mathbf{B}\right]_{2M}\mathbf{Q}=\mathbf{0} \tag{39}$$

where $\mathbf{Q}=\begin{bmatrix}\mathbf{\Phi}\\ \xi\mathbf{\Phi}\end{bmatrix}$. **A** and **B** are known matrices for fixed values of the circular frequency ω. Their explicit expression is:

$$\mathbf{A}=\begin{bmatrix}\mathbf{0} & \mathbf{K}_1-\omega^2\,\mathbf{M}^{g}\\ \mathbf{K}_1-\omega^2\,\mathbf{M}^{g} & i\mathbf{K}_2\end{bmatrix},\qquad B=\begin{bmatrix}\mathbf{K}_1-\omega^2\,\mathbf{M}^{g} & \mathbf{0}\\ \mathbf{0} & -\mathbf{K}_3\end{bmatrix}. \tag{40}$$

The solution of Eq. (39) is given in terms of eigenvalues ξ and eigenvectors **Q**. While the eigenvectors are complex, the eigenvalues can be pairs of real numbers ($\pm\xi_{Re}$) representing propagating waves in the ± x directions, pairs of complex conjugate numbers ($\pm\xi_{Re}\pm i\,\xi_{\mathrm{Im}}$) representing evanescent waves decaying in the $\pm x$ directions, or pairs of purely imaginary numbers ($\pm i\,\xi_{\mathrm{Im}}$) representing non oscillating evanescent waves in the $\pm x$ directions (Hayashi et al. 2003). The corresponding mode shape $\mathbf{\Phi}$ can be extracted as the upper part of vector **Q**, while the associated attenuation, phase (c_p) and group (c_g) velocities can be obtained as

$$att=\xi_{\mathrm{Im}} \tag{41}$$

$$c_p = \omega / \xi_{Re} \tag{42}$$

$$c_g = \frac{\partial \omega}{\partial \xi} = \frac{\mathbf{\Phi}_L^T \left(i\mathbf{K}_2 + 2\xi \mathbf{K}_3 \right) \mathbf{\Phi}_R}{2\omega \, \mathbf{\Phi}_L^T \mathbf{M}^g \mathbf{\Phi}_R} \tag{43}$$

with $\mathbf{\Phi}_L$ and $\mathbf{\Phi}_R$ indicating the left and right mode shapes respectively.

The knowledge of the velocities for each ω-ξ pair allows to build the dispersion curves. It is also important for the purposes of this topic to "follow" a given wave mode at varying frequencies. In order to do that, the results in this paper adopt the B-orthogonality wave mode sorting algorithm originally proposed by Loveday and Long (2007). Since at the same frequency ω, two eigenvectors r and s obtained from Eq. (39) must respect the orthogonality condition with the **B** matrix, the same condition can be assumed for the next frequency step$\left(\omega + \Delta\omega\right)$, allowing to "follow" or "track" the mode during frequency sweeping according to:

$$\mathbf{Q}_r^T \left(\omega\right) \mathbf{B} \mathbf{Q}_s \left(\omega + \Delta\omega\right) \cong \begin{cases} 0 & if\ r \neq s \\ \neq 0 & if\ r = s \end{cases} . \tag{44}$$

2.5 *Energy calculations*

The soundness of the proposed GL method can be validated by verifying the conservation of energy between the incident mode and the scattered (reflected and transmitted) modes:

$$E_{in} = \sum_{j=1}^{N_M} \left(E_{\mathrm{Refl}}^{(j)} + E_{Transm}^{(j)} \right) \tag{45}$$

where E_{in}, $E_{\mathrm{Refl}}^{(j)}$, $E_{Transm}^{(j)}$ are the energy fluxes of the incident wave and of the j-th reflected and transmitted waves, respectively.

The energy flux carried by the propagating mode j in the **n** direction over a unit period of time through the cross-sectional area Γ can be evaluated as:

$$E^{(j)} = \int_\Gamma \mathbf{P}^{(j)} \bullet \mathbf{n} \, d\Gamma , \tag{46}$$

where

$$\mathbf{P}^{(j)} = -\frac{1}{2} \mathrm{Re} \left[\boldsymbol{\sigma}^{(j)} \bar{\dot{\mathbf{u}}}^{(j)} \right] \tag{47}$$

is the Poynting vector, with $\boldsymbol{\sigma}$ the stress tensor in matrix form notation and $\bar{\dot{\mathbf{u}}}$ the complex conjugate velocity vector.

Substitution of Eq. (47) into Eq. (46) allows to rewrite Eq. (46) in Voigt notation as

$$E^{(j)} = -\frac{1}{2} \int_\Gamma \mathrm{Re} \left[\left(\mathbf{L}_n^T \boldsymbol{\sigma} \right)^T \bar{\dot{\mathbf{u}}} \right] d\Gamma . \tag{48}$$

By taking into account the harmonic time dependence of $\boldsymbol{\sigma}$ and $\mathbf{u}$ and considering the particular case of waves travelling in the x direction, the energy term for the j-th mode becomes:

$$E^{(j)} = -\frac{\left|A_j\right|^2}{2}\mathrm{Re}\left[i\omega\mathbf{F}^{(j)^T}\bar{\mathbf{\Phi}}^{(j)}\right] \tag{49}$$

where $\mathbf{\Phi}^{(j)}$ and $\mathbf{F}^{(j)}$ are the nodal displacements and correspondent consistent forces for mode j according to the adopted FE discretization.

3. Case study: scattering of guided waves in skin-to-stringer assembly of composite aircraft panels

The GL formulation described above was implemented in a Matlab© code. The code was designed to calculate the response within a fixed frequency range of the incoming wave and for a fixed number of frequency steps. The general numerical procedure is schematized in Fig. 2.

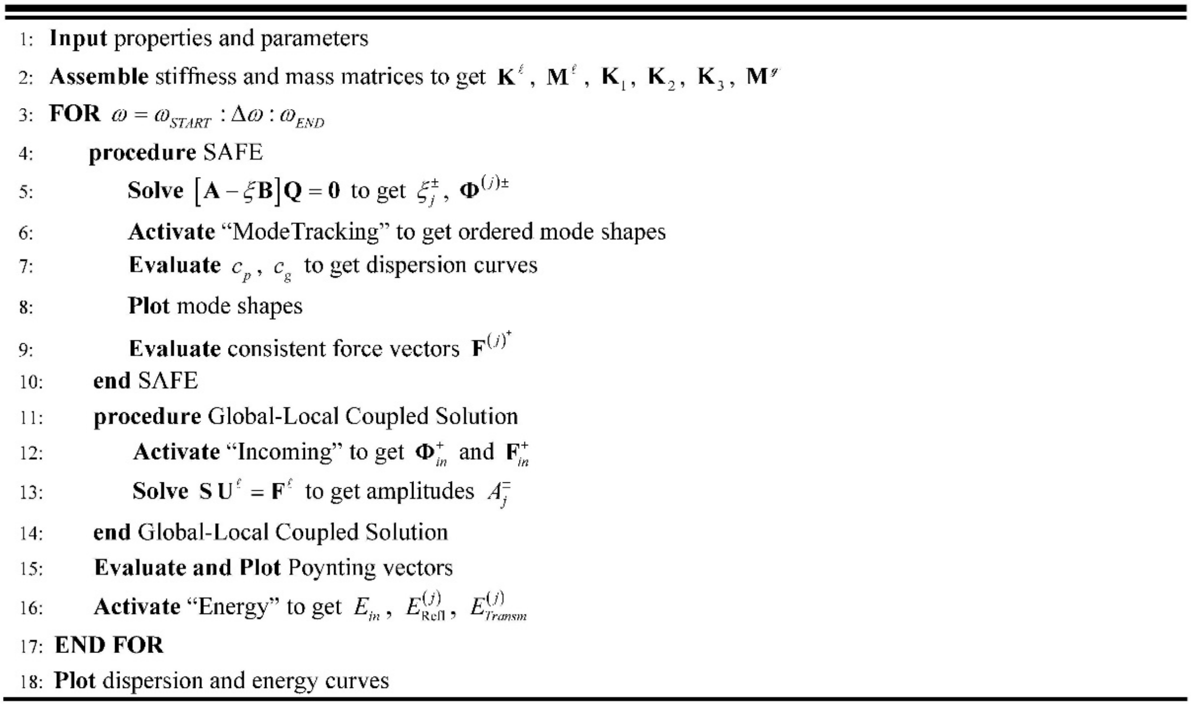

```
Input properties and parameters
Assemble stiffness and mass matrices to get $\mathbf{K}^{\ell}$, $\mathbf{M}^{\ell}$, $\mathbf{K}_1$, $\mathbf{K}_2$, $\mathbf{K}_3$, $\mathbf{M}^{g}$
FOR $\omega = \omega_{START} : \Delta\omega : \omega_{END}$
    procedure SAFE
        Solve $[\mathbf{A} - \xi\mathbf{B}]\mathbf{Q} = \mathbf{0}$ to get $\xi_j^{\pm}$, $\mathbf{\Phi}^{(j)\pm}$
        Activate "ModeTracking" to get ordered mode shapes
        Evaluate $c_p$, $c_g$ to get dispersion curves
        Plot mode shapes
        Evaluate consistent force vectors $\mathbf{F}^{(j)^+}$
    end SAFE
    procedure Global-Local Coupled Solution
        Activate "Incoming" to get $\mathbf{\Phi}_{in}^{+}$ and $\mathbf{F}_{in}^{+}$
        Solve $\mathbf{S}\,\mathbf{U}^{\ell} = \mathbf{F}^{\ell}$ to get amplitudes $A_j^{-}$
    end Global-Local Coupled Solution
    Evaluate and Plot Poynting vectors
    Activate "Energy" to get $E_{in}$, $E_{\mathrm{Refl}}^{(j)}$, $E_{Transm}^{(j)}$
END FOR
Plot dispersion and energy curves
```

Fig. 2. Key steps of the Matlab GL code.

The geometry of the case study is shown in Fig. 3, and represents a scaled version of a skin-to-stringer assembly found in commercial aircraft construction. This structure is being considered for ultrasonic guided-wave inspection (Capriotti et al., 2017). Scattering results for typical incoming wave modes were obtained for a "pristine" case and for four "damage" cases representing relevant defects in this structure. These predictions can allow to best target the inspection to a particular defect and/or to quantitatively relate a measured scattering behavior to a particular defect.

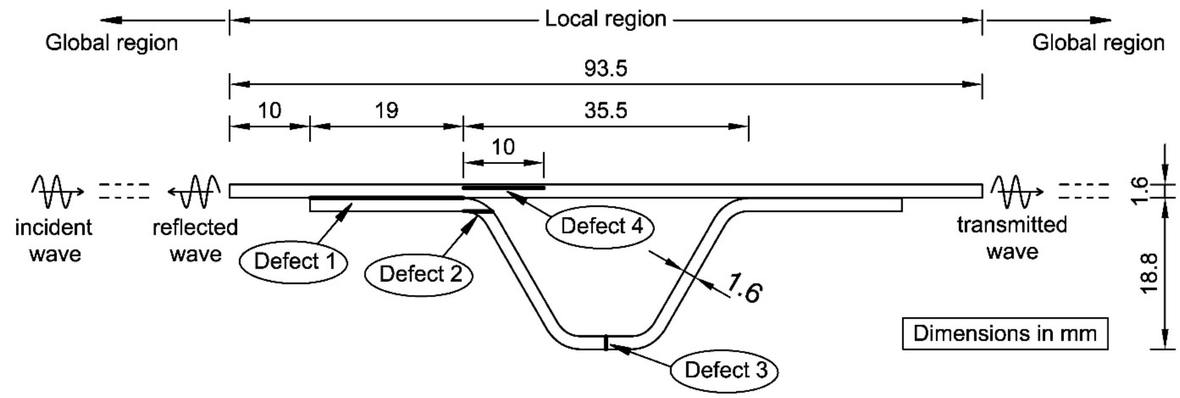

Fig. 3. Global-Local model of the composite skin-to-stringer assembly, with the four "defected" configurations: delamination between skin and stringer (Defect 1), horizontal fracture in the stringer heel (Defect 2), vertical fracture in the stringer cap (Defect 3), and delamination between 2nd and 3rd laminae in the skin (Defect 4).

In the model, the skin and the hat-shaped stringer are both 8-layers of $[0/+45/-45/0]_S$ carbon-epoxy unidirectional laminae with a total thickness of 1.6 mm. An additional 0° lamina is placed at the interface between skin and stringer. The zero degree lamina direction corresponds to the out-of-plane direction of the 2D drawing in Fig. 3. The density of each lamina is 1530 kg/m^3 and the elastic properties in the principal direction of material symmetry are given in Table 1 (assuming transverse isotropy), where *1* is the fiber direction, *2* is the direction perpendicular to the fibers in the lamina plane, and *3* the through-thickness direction.

Table 1. Elastic properties for the CFRP lamina

Property	C_{11}	C_{12}	C_{13}	C_{22}	C_{23}	C_{33}	C_{44}	C_{55}	C_{66}
GPa	135	5.70	5.70	14.20	8.51	14.20	2.87	4.55	4.55

Shown in Fig. 3, the "local" region was extended to include 10 mm on either side of the stringer, in order to limit any role of evanescent modes when computing reflection and transmission spectra. A total of 12376 quadrilateral 2-D isoparametric linear elements (5952 for the skin and 6424 for the stringer) were used for the local discretization, for a total number of local FE nodes of 13022. On the "global" side, for computational consistency, two 1D isoparametric linear elements were used for each lamina, for a total of 16 elements and 17 nodes. Four Gauss points were used for the quadrature of the 2D elements, and 2 Gauss points for the 1D elements. The maximum size of the elements was $L = 0.26$ mm, in order to satisfy the following customary meshing criterion:

$$\lambda_T > \beta L \tag{50}$$

where $\lambda_T = 2\pi c_T / \omega$ is the wavelength of transverse waves at frequency ω traveling at bulk shear velocity c_T. With linear elements, values of $\beta = 10$ (Chang and Mal, 1995) or $\beta = 20$ (Bartoli et al., 2005; Galan and Abascal, 2005) are customary. For the case of quadratic elements, a value of $\beta = 4$ was utilized. All analyses were run using a Core i7 CPU with 64 GB of RAM, in the frequency range of DC-500 kHz, with steps of 5 kHz. The incident wave source distance was $d_s = 0.25$ m from the middle of the stringer (origin of the reference system) on the left side of the drawing in Fig. 3.

3.1 Code pre-validation: skin-only model (composite laminate)

An initial validation of the accuracy of the proposed GL algorithm was conducted on a simpler geometry of a pristine multi-layered composite plate corresponding to the skin only of Fig. 3. This analysis was done to check the generation of the dispersion curves and wave energy conservation in the scattering process.

From the SAFE portion of the GL code, the results in terms of phase velocity and group velocity dispersion curves in the DC-500 kHz frequency range are presented in Fig. 4a and Fig. 4b, respectively. Four modes appear in this range, including three fundamental modes (m_1, m_2 and m_3) and a higher-order mode (m_4) with cut-off frequency ~450 kHz. As expected, the curves are generally similar to the Rayleigh-Lamb dispersion curves of isotropic plates, with m_1 corresponding to the zero-order flexural (A_0) Lamb mode, m_2 corresponding to the zero-order axial (S_0) Lamb mode, m_3 to the zero-order shear horizontal (SH_0) Lamb mode, and m_4 to the first-order flexural (A_1) Lamb mode.

For the remainder of the paper, the attention will be focused on the flexural and the axial modes since they are the ones most commonly utilized in guided-wave testing of composite or metal plates.

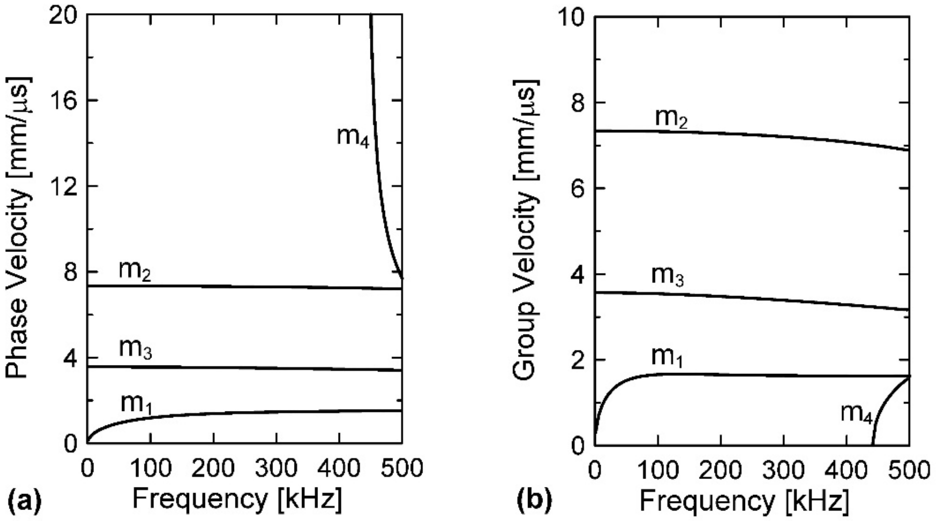

Fig. 4. (a) Phase velocity dispersion curves and (b) group velocity dispersion curves for the $[0/+45/-45/0]_S$ CFRP composite laminate (skin only) from the SAFE portion of the GL code.

The energy conservation check for the transmission (Transm) and reflection (Refl) scattering processes was performed for the two cases of incident m_1 (flexural) mode and incident m_2 (axial) mode according to Eq. (45) of the GL formulation. In particular, the left boundary of the local region in the schematic of Fig. 3 was used for the computation of the reflected waves, and the right boundary of the local region in Fig. 3 was used for the computation of the transmitted waves.

Fig. 5a shows the scattering spectra for the case of m_1 incident. As expected, due to the absence of discontinuities or geometrical asymmetries in the pristine composite skin, the same mode m_1 is entirely transmitted and no mode is reflected (total transmission) throughout the frequency range. The same result is obtained for the case of m_2 incident, shown in Fig. 5(c), that again shows the total m_2 transmission with no reflections. In addition, the scattering spectra in both cases have a constant unity amplitude that corresponds to the incident energy, demonstrating energy conservation. These results give confidence on the accuracy of the GL model for the skin structure. The fact that no spurious reflections are seen at the higher frequency values also gives reassurance on the level of mesh discretization adopted.

The energy distribution for the incident modes across the laminate thickness is shown in Fig. 5(b) for the m_1 mode and in Fig. 5(d) for the m_2 mode. These figures plot the values of the Poynting vector along the wave propagation direction, x, at the Gauss points. Energy distributions recorded at the left and the right boundaries coincide with those of the incoming mode, as expected in pristine conditions. These cross-sectional energy plots shine light on the different "nature" of the incident modes, with the m_1 (flexural) mode focusing its energy on the outer plies of the laminate, and the m_2 (axial) mode affecting both outer plies and inner plies of the laminate. It is known (e.g. Matt et al. 2005) that these distributions control how different modes interact with adjacent components (e.g. the stringer) and with skin defects located at different depths.

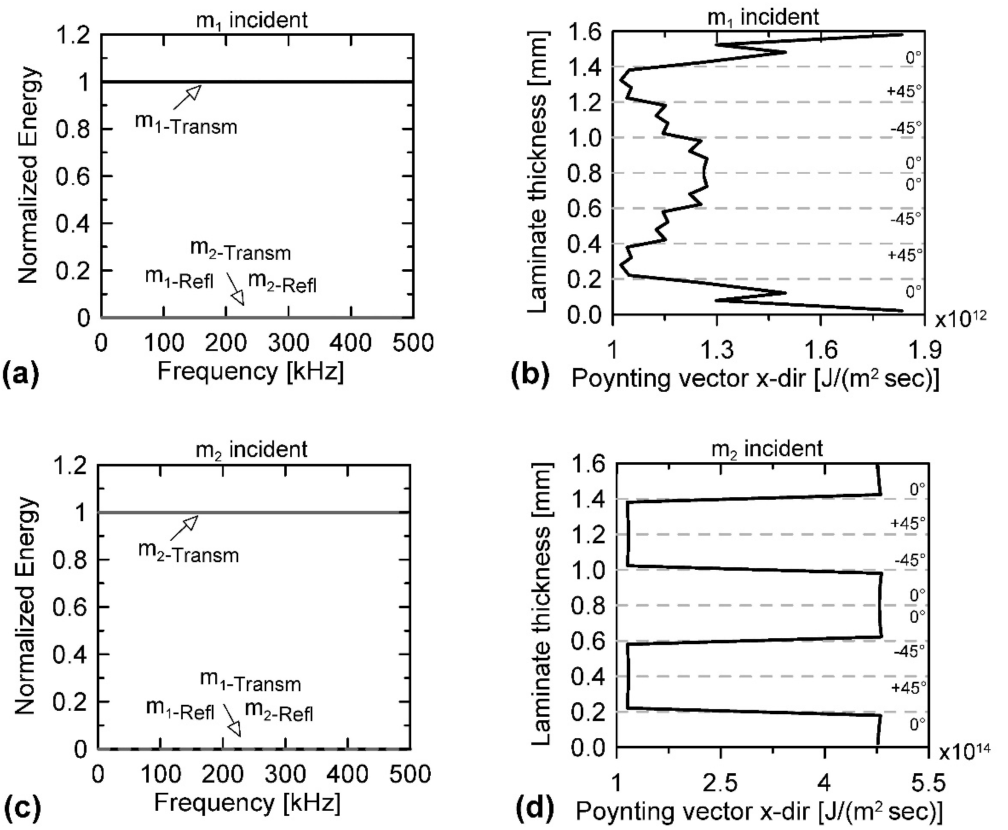

Fig. 5. Skin laminate: (a) Transmission and reflection energy spectra and (b) cross-sectional energy (Poynting vector) in the case of an m_1 incident mode. (c) Transmission and reflection energy spectra and (d) cross-sectional Poynting vector in the case of an m_2 incident mode.

3.2 Results from composite skin-to-stringer assembly

The next Global-Local analysis was conducted on the full skin-to-stringer assembly of Fig. 3. The goal was to predict scattering spectra in this system for the case of a pristine assembly, and four different defects as shown in Fig. 3. These defects consisted of: delamination between skin and stringer (Defect 1), horizontal fracture in the stringer (Defect 2), vertical fracture in the stringer (Defect 3), and delamination between 2nd and 3rd laminae in the skin (Defect 4). Defects 1, 2 and 3 were modelled by removing some of the elements from the mesh; Defect 4 was modelled by doubling the nodes and physically separating the elements between the second and third layer for the length specified in Fig. 3.

3.2.1 Pristine skin-to-stringer assembly

The addition of the hat-shaped stringer to the skin laminate significantly increases the complexity of the scattering problem. Key results from the GL model of the pristine assembly are shown in Figs. 6 and 7 for the cases of incident m_1 (flexural) mode and incident m_2 (axial) mode.

Fig. 6a shows the scattering spectra (reflections and transmission) in the DC-500 kHz frequency range for an incident m_1 mode. As for the skin-only results, the reflection spectra are computed at the left boundary of the local region and the transmission spectra are computed at the right boundary of the local region. As before, the total energy is computed adding up the transmitted and reflected energy for all the modes, considering a unity incoming mode. Fig. 6a shows a computed total energy spectrum flat and close to 1, which satisfies conservation of energy to within very small numerical errors caused by the FE discretization and the normal mode decomposition. The same figure also shows that, when m_1 is incident, the majority of the energy is transmitted through the skin-to-stringer assembly and reflected back into the skin as the same mode m_1, with very little mode conversion into m_2. This is true at most frequencies, except for specific frequencies such as 105 kHz, 200 kHz, 260-320 kHz and 450-470 kHz, where the mode-converted m_2 is transmitted through the overall structure more than m_1. The lower frequency range (up to 200 kHz) is very sensitive to m_1, reaching more than an 80% of transmission, with transmission peaks at ~ 50 kHz and ~ 135 kHz. These values could therefore be ideal excitation frequencies for a pitch-catch guided-wave inspection that uses m_1 in transmission. Conversely, 90% of the m_1 energy is reflected in the high frequency range (~360-460 kHz) that can instead be considered for a pulse-echo guided-wave test using reflection measurements. The spectra in Fig. 6a also reveal interesting m_1-m_2 mode-conversion bands, such as the m_2 transmission in the ~ 260-320 kHz range and the m_2 reflection around 200 kHz. The mode conversion information can also be extremely useful in a practical guided-wave test. The higher-order mode m_4 appears with a very small contribution above its cut-off frequency of 450 kHz.

The corresponding case of an m_2 incident mode is shown in Fig. 6b. The spectra identify specific frequency ranges for predominant transmission or reflection behaviour, as well as m_2-m_1 mode conversion opportunities. For example, significant mode conversion into both transmitted m_1 and reflected m_1 occur in the 150-350 kHz range, as well as at some other individual frequencies revealed by the energy peaks. The plot also shows the small contribution of the higher-order mode m_4 above 450 kHz.

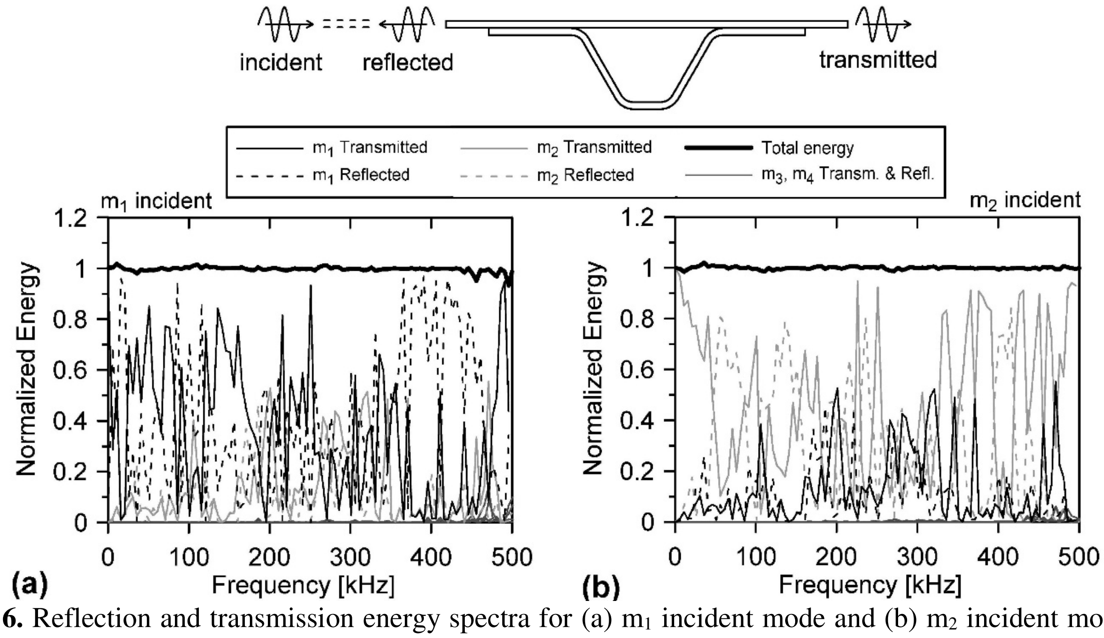

Fig. 6. Reflection and transmission energy spectra for (a) m_1 incident mode and (b) m_2 incident mode in the skin-to-stringer pristine assembly.

In order to shine additional light on these behaviours, Fig. 7 shows results obtained when zooming into the two salient frequency values of 150 kHz and 200 kHz. For an m_1 incident mode, for example, the spectra in Fig. 7a shows that at 150 kHz most of the energy is transmitted as the same mode m_1. This result is best explained by the cross-sectional energy distribution (Poynting vector along x) shown in Fig. 7b that confirms the same energy shapes at the left boundary and at the right boundary, i.e. little or no disturbance to the nature of the m_1 mode as it crosses through the stringer at this frequency. Conversely, at a 200 kHz frequency, the spectra for the incident m_1 mode in Fig. 7a shows considerable (50%) mode conversion into an m_2. This different behaviour is again explained by the cross-sectional energy plots of Fig. 7c that show how the m_1 cross-sectional shape at the left boundary changes into an m_2 shape at the right boundary after traveling through the stringer (see also Fig. 5).

If m_2 is used as the incoming mode, at 150 kHz Fig. 7d shows a 50-50 split between transmission and reflection. The Poynting vector plots of Fig. 7e at 150 kHz confirms this behaviour, showing a split of incoming energy into the left boundary and the right boundary. At 200 kHz, instead, significant m_2 – m_1 mode conversion takes place (as seen in the previous m_1 incoming case), as confirmed by the Poynting vectors of Fig. 7f showing a change from m_2 distribution at the left boundary into an m_1 distribution at the right boundary after travelling through the stringer.

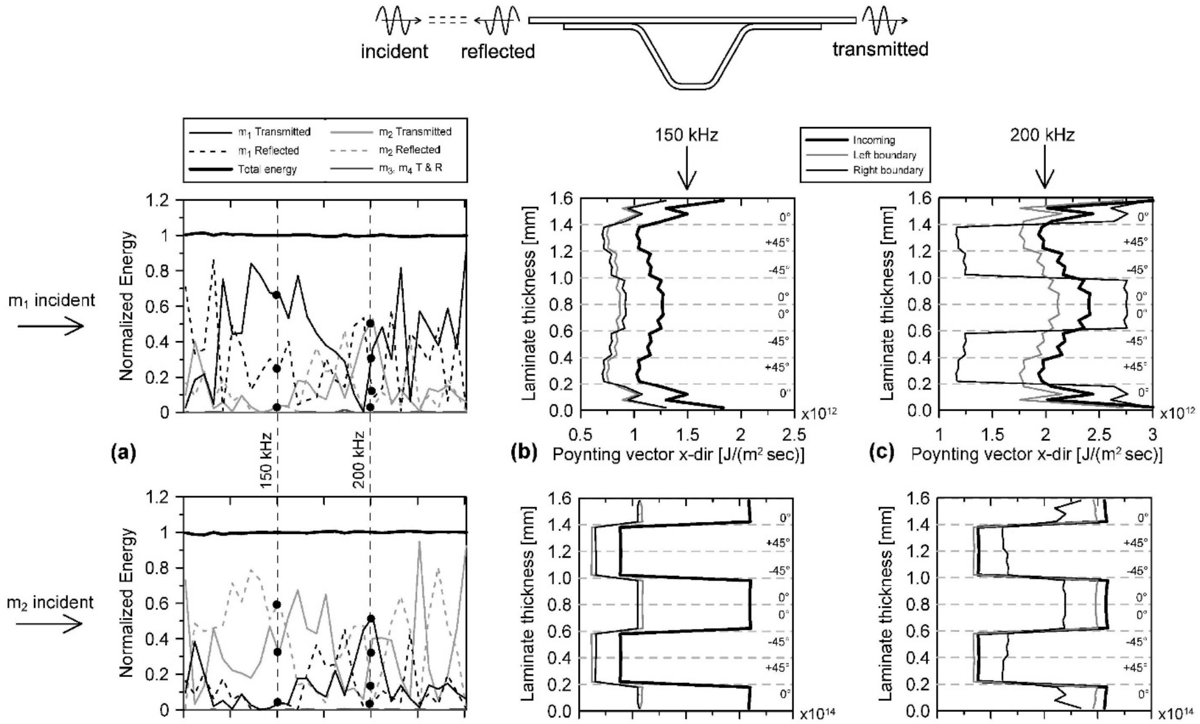

Fig. 7. Scattering behaviour at specific frequencies (pristine skin-to-stringer assembly). (a) Zoomed scattering spectra for the m_1 incident mode with cross-sectional energy (Poynting vector) at 150 kHz (b) and at 200 kHz (c). Corresponding results for the m_2 incident mode in (d), (e) and (f).

3.2.2 Damaged skin-to-stringer assembly

The interest in the GL scattering modeling of the “damaged” skin-to-stinger assembly is to explore defect-mode sensitivities in specific frequency ranges in ways that cannot be obtained from theoretical considerations due to the material and geometrical complexity of the scattering problem. In this section scattering spectra from the GL method are shown for the various defects considered. For the sake of compactness, the results are shown for the transmission behaviour only and considering possible mode conversions. This is done in analogy with a pitch-catch guided-wave testing approach of the type experimentally utilized for a similar structure by Capriotti et al. (2017). In order to better isolate the role of each defect, the calculations are shown in terms of <defect - pristine> “difference” spectra. Negative values in the difference spectra correspond to wave energy absorptions caused by the defect, whereas positive values in the difference spectra correspond to enhanced wave transmission caused by the defect.

The results for Defect 1 (skin-to-stringer delamination) are shown in Fig. 8. This delamination was simulated by eliminating the transition lamina at the left side of the interface. If the flexural m_1 is used as the incoming mode (Fig. 8a), frequencies in the 85-420 kHz range show a good sensitivity to this defect. In particular, for example, significant m_1 wave energy absorption (negative peaks in the difference spectrum) can be expected at 160 kHz (70% absorption), 250 kHz and 350 kHz. Conversely, increased m_1 energy transmission (as high as 70% increase) can be expected at 90 kHz and 290 kHz. The transmission of the axial mode m_2, Fig. 8d, is also found quite sensitive to this defect. The figure for m_2 transmission shows significant absorption peaks (up to 90%) in the higher frequency range 250-450 kHz, and significant transmission peaks (up to 85%) in the lower frequency range of 50-250 kHz. The stronger transmission at certain frequencies can be intuitively explained by the fact that skin-stringer delamination eliminates wave energy leakage into the stringer and thus confines the wave transmission to the skin only. The mode conversion transmission spectra are also shown in Fig. 8b and 8c. These plots reveal specific ranges of opportunity for detecting the damage through mode conversion, such as the 200-400 kHz range where several absorption peaks are present. In an actual test, these mode-frequency ranges can be exploited to optimally detect this kind of defect.

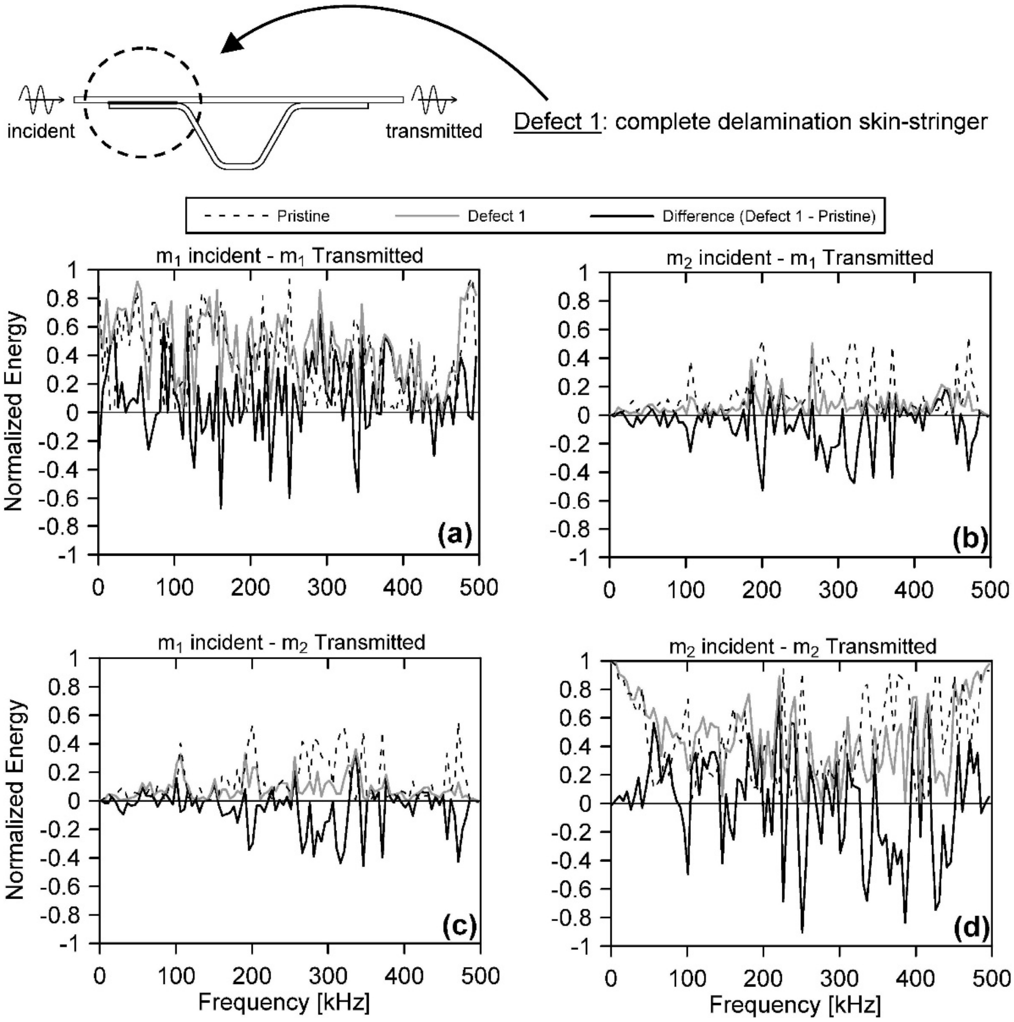

Fig. 8. Defect 1 case (skin-stringer delamination). Wave transmission spectra for pristine, defect and (defect-pristine) difference for (a) m_1 incident - m_1 transmitted; (b) m_2 incident - m_1 transmitted (mode conversion); (c) m_1 incident – m_2 transmitted (mode conversion), and (d) m_2 incident – m_2 transmitted.

The case of the stringer heel crack defect (Defect 2) is shown in Fig. 9, where the schematic depicts the simulated fracture at the top-left corner of the stringer. The transmitted flexural m_1 energy for the same m_1 incoming mode (Fig. 9a) shows good sensitivity particularly in the lower frequency range DC-250 kHz as well as around 350 kHz, where the negative difference spectrum indicates energy absorption (up to 90% at 250 kHz) induced by this defect. Increased transmission (positive difference spectrum) on the order of 50% is instead predicted at specific frequency values such as 115 kHz and 195 kHz. The transmitted axial m_2 mode under the same incoming m_2 mode (Fig. 8d) is also quite sensitive to this defect, with wave energy absorption as high as 90% in the 350 – 450 kHz range, and increased transmissions up to 50% in other frequency ranges. The mode conversion spectra of m_2 incident-m_1 transmitted (Fig. 8b) and m_1 incident-m_2 transmitted (Fig. 8c) generally show less sensitivity to this defect than the same-mode spectra, with maximum ~40% energy absorption in the 200 – 350 kHz range.

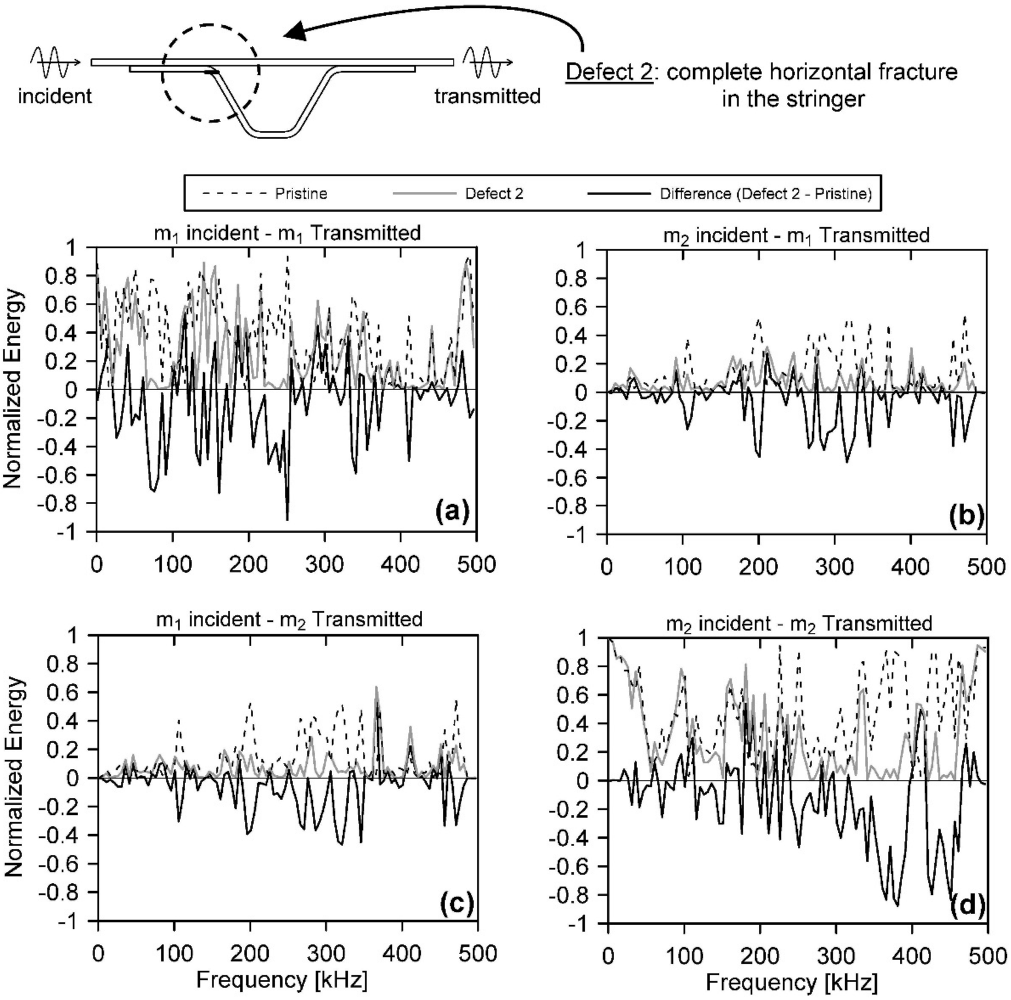

Fig. 9. Defect 2 case (stringer heel crack). Wave transmission spectra for pristine, defect and (defect-pristine) difference for (a) m_1 incident - m_1 transmitted; (b) m_2 incident - m_1 transmitted (mode conversion); (c) m_1 incident – m_2 transmitted (mode conversion), and (d) m_2 incident – m_2 transmitted.

The case of the stringer cap crack (Defect 3) is shown in Fig. 10. The transmission spectra are similar to those obtained for the Defect 2 case: the flexural m_1 - m_1 combination (Fig. 10a) is most sensitive in the low frequency range DC-200 kHz, while the axial m_2 – m_2 combination (Fig. 10d) is mostly sensitive in the higher frequency range of 250-450 kHz. In these ranges, both combinations show significant energy absorption (as high as ~ 90%) caused by the defect. The mode-converted spectra of m_2 – m_1 (Fig. 10b) and m_1 – m_2 (Fig. 10c) for Defect 3 are also similar to those of Defect 2, with smaller sensitivity compared to the same-mode spectra. One notable difference between the two stringer damage cases is the same-mode transmission spectrum around 250 kHz, where the stringer heel crack Defect 2 causes 90% absorption for the m_1 - m_1 combination (Fig. 9a) that does not occur for the stringer cap crack Defect 3 (Fig. 10a); the opposite occurs for the m_2 – m_2 combination at 250 kHz, where the stringer cap crack Defect 3 produces 90% absorption (Fig. 10d) that is much reduced for the stringer heel crack Defect 2 (Fig. 9d). These kinds of considerations can help selecting specific mode-frequency combinations and/or interpreting results of guided-wave measurements in these structures.

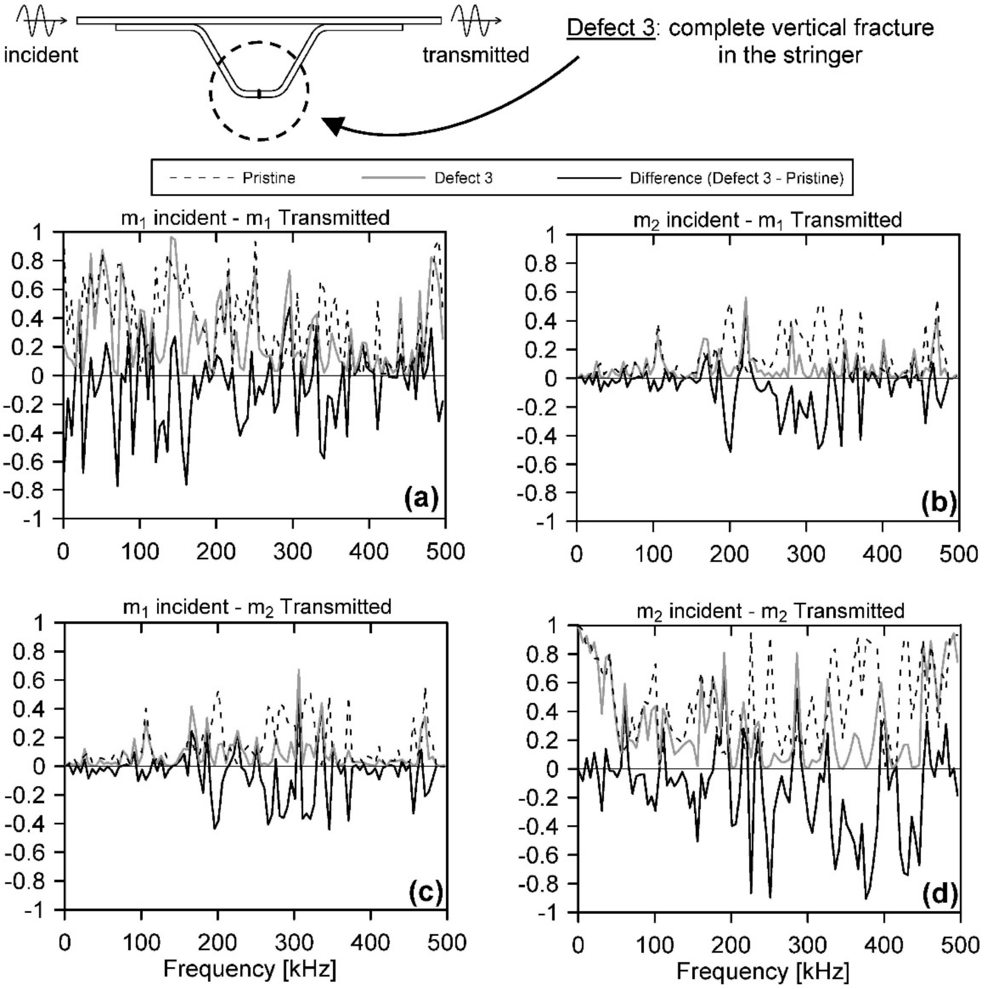

Fig. 10. Defect 3 case (stringer cap crack). Wave transmission spectra for pristine, defect and (defect-pristine) difference for (a) m_1 incident - m_1 transmitted; (b) m_2 incident - m_1 transmitted (mode conversion); (c) m_1 incident – m_2 transmitted (mode conversion), and (d) m_2 incident – m_2 transmitted.

The last defect that was considered is the skin delamination (Defect 4), that was inserted between the 2nd and the 3rd layer of the composite skin laminate as schematized in Fig. 11. In this case, a very sensitive combination is the same mode flexural m_1 - m_1 (Fig. 11a), with significant energy absorption throughout the entire frequency range and absorption peaks of 70% at 80 kHz and 210 kHz. Interestingly, the axial m_2 – m_2 combination (Fig. 11d) is only sensitive to this delamination in the high frequency range above 400 kHz, with a peak 80% absorption at 425 kHz. This result is expected by the rule of thumb consideration of ultrasonic testing where higher frequencies are more sensitive due to the smaller wavelength-to-defect size ratios. However, the full GL analysis presented here reveals a much more complete picture of mode sensitivities, with specific “sensitive” mode-frequency combinations also at the lower frequencies (e.g. in the aforementioned m_1 - m_1 combination). Since the skin delamination breaks the geometrical symmetry of the skin, it creates some m_2 – m_1 and m_1 – m_2 mode conversions, shown in Figs. 11b and 11c, particularly in the 250-350 kHz range. The mode conversions in this frequency range could also be utilized to detect this kind of defect in an actual inspection test.

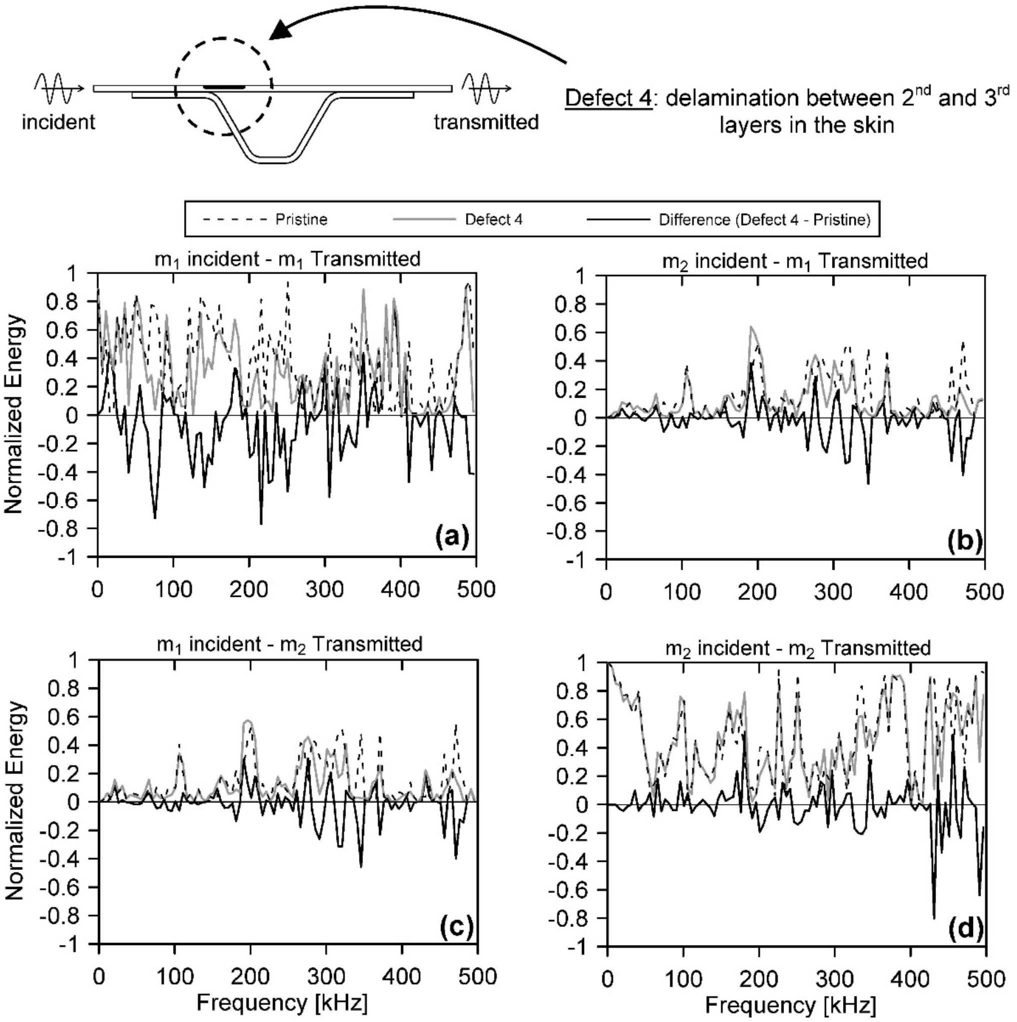

Fig. 11. Defect 4 case (skin delamination). Wave transmission spectra for pristine, defect and (defect-pristine) difference for (a) m_1 incident - m_1 transmitted; (b) m_2 incident - m_1 transmitted (mode conversion); (c) m_1 incident – m_2 transmitted (mode conversion), and (d) m_2 incident – m_2 transmitted.

4. Discussion and Conclusions

This paper has addressed the problem of scattering of multimode and dispersive elastic waves propagating in waveguide geometries. Among other applications, this topic is of great interest to ultrasonic guided-wave NDT or SHM of structural components where defects are detected by recording transmission or reflection scattering of a generated incoming wave mode. Predictions of these scattering patterns for a given defect can allow to select optimum mode-frequency combinations for the incoming mode, and/or to identify the type of defect being detected by a specific scattering observation.

For general cases that are complex in terms of either geometry or material properties (or both), this problem requires a numerical solution. A unified Global – Local (GL) approach has been presented here, exploiting the computational efficiency of the Semi-Analytical Finite Element (SAFE) technique for a cross-sectional discretization of the "global" portion, coupled with a full Finite Element discretization of the "local" portion containing the scatterer. Compared to previous GL studies, this contribution adds: (a) a general and consistent formulation for the evaluation of the nodal tractions at the global-local boundaries; (b) the implementation of a robust mode tracking control, based on B-orthogonality, for the automatic selection of incoming and scattered modes; (c) the possibility to model a wide frequency range also including higher-order modes; (d) the automatic inclusion of an energy balance check in the results; and (e) the unification of SAFE and FE in a stand-alone numerical Matlab code that is readily extendable to more general cases (e.g. independent treatment of the two global regions, explicitly given theoretical formulation such as consistent nodal forces at the boundaries, or extension to 3D cases).

The proposed GL algorithm was applied to a composite skin-to-stringer assembly typical of commercial aircraft construction. Various relevant defects were modelled, and scattering spectra were obtained for guided-wave frequencies as high as 500 kHz under incoming flexural (A_0-type) or axial (S_0-type) modes that are typically employed as excitations in guided-wave testing of these components. The results reveal quite interesting transmission spectra, same-mode or mode-converted, that are peculiar to each of the defects considered. These predictions can be extremely useful to guide and interpret guided-wave inspection tests conducted on these components.

Although the GL formulation presented applies to a general 3D case, the case study considered was a 2D (plain strain) analysis that is quite applicable to a scanning-type guided-wave system of the type utilized by Capriotti et al. (2017). An extension to a 3D scattering case for internal flaws in railroad tracks using this algorithm is being currently studied by the authors.

The results shown for the skin-to-stringer case study only apply to the specific geometry and material properties considered. However, the cross-sectional mode shapes mostly control the partition of energy between the incoming mode and the scattered modes. Consequently, some scalability of the results to components of different thicknesses can be qualitatively predicted on the basis of the well-known invariance of the guided-wave cross-sectional mode shapes with the <frequency × thickness> product (Rose 2014). In other words, for the same mode shape to be generated, frequency and thickness must be inversely proportional. As a result, for example, specific frequency values of interest in the scattering spectra predicted for a given thickness of the skin could be scaled to a different skin thickness, provided that the <frequency × thickness> product is the same.

The paper has considered elastic waves with no viscoelastic damping. Damping could be included by considering complex stiffness matrices in the analysis resulting in complex wavenumbers as discussed, for example, by Bartoli et al. (2006). The inclusion of damping would affect the predicted scattering spectra mostly in amplitude, with presumably small shifts in peak frequency positions since those are mostly controlled by cross-sectional mode shapes (that should not change significantly with damping). Extensions of the skin-to-stringer case study that include damping will be considered in future works.

Acknowledgements

Part of this work was funded by the Federal Aviation Administration Joint Center of Excellence for Advanced Materials (FAA Cooperative Agreement 12-C-AM-UCSD). A. Spada was financially supported by the Fulbright Program for the fulfilment of the project E0584038 “Analytical-Numerical models for the simulation of ultrasonic guided wave propagation in composite structures”. The opportunity given by the Fulbright Program is greatly acknowledged.

References

Ahmad, Z. A. B., Vivar-Perez, J. M., Gabbert, U., 2013. Semi-analytical finite element method for modeling of lamb wave propagation. *CEAS Aeronautical Journal*, *4*(1), 21-33.

Al-Nassar, Y. N., Datta, S. K., Shah, A. H., 1991. Scattering of Lamb waves by a normal rectangular strip weldment. *Ultrasonics*, *29*(2), 125-132.

Bartoli, I., Lanza di Scalea, F., Fateh, M., Viola, E., 2005. Modeling guided wave propagation with application to the long range defect detection in railroad tracks. *NDT&E International*, 38, 325-334.

Bartoli, I., Marzani, A., di Scalea, F. L., Viola, E., 2006. Modeling wave propagation in damped waveguides of arbitrary cross-section. *Journal of Sound and Vibration*, *295*(3-5), 685-707.

Capriotti, M., Kim, H. E., Lanza di Scalea, F., Kim, H., 2017. Non-Destructive inspection of impact damage in composite aircraft panels by ultrasonic guided waves and statistical processing. *Materials*, *10*(6), 1-12.

Castaings, M., Le Clezio, E., Hosten, B., 2002. Modal decomposition method for modeling the interaction of Lamb waves with cracks. *The Journal of the Acoustical Society of America*, *112*(6), 2567-2582.

Chang, Z., Mal, A. K., 1995. A global-local method for wave propagation across a lap joint. *ASME Applied Mechanics Division Publications AMD, 204*, 1-1.

Chang, Z., Mal, A.,1999. Scattering of Lamb waves from a rivet hole with edge cracks. *Mechanics of materials*, *31*(3), 197-204.

Datta, S. K., Ju, T. H., Shah, A. H., 1992. Scattering of an impact wave by a crack in a composite plate. *Journal of Applied Mechanics*, *59*(3), 596-603.

Datta, S. K., Shah, A. H., Bratton, R. L., Chakraborty, T., 1988. Wave propagation in laminated composite plates. *The Journal of the Acoustical Society of America*, *83*(6), 2020-2026.

Dong, S.B., Goetschel, D.B., 1982. Edge effects in laminated composite plates. *Journal of Applied Mechanics*, 49, 129-135.

Galán, J. M., Abascal, R., 2002. Numerical simulation of Lamb wave scattering in semi-infinite plates. *International Journal for Numerical Methods in Engineering*, *53*(5), 1145-1173.

Galán, J. M., Abascal, R., 2005. Boundary element solution for the bidimensional scattering of guided waves in laminated plates. *Computers & structures*, *83*(10-11), 740-757.

Goetschel, D. B., Dong, S. B., Muki, R., 1982. A global local finite element analysis of axisymmetric scattering of elastic waves. *Journal of Applied Mechanics*, *49*(4), 816-820.

Guo, N., Cawley, P., 1993. The interaction of Lamb waves with delaminations in composite laminates. *The Journal of the Acoustical Society of America*, *94*(4), 2240-2246.

Haider, M. F., Bhuiyan, M. Y., Poddar, B., Lin, B., Giurgiutiu, V., 2018. Analytical and experimental investigation of the interaction of Lamb waves in a stiffened aluminum plate with a horizontal crack at the root of the stiffener. *Journal of Sound and Vibration*, *431*, 212-225.

Hayashi, T., Song, W. J., Rose, J. L., 2003. Guided wave dispersion curves for a bar with an arbitrary cross-section, a rod and rail example. *Ultrasonics*, *41*(3), 175-183.

Karim, M. R., Awal, M. A., Kundu, T., 1992. Elastic wave scattering by cracks and inclusions in plates: in-plane case. *International Journal of Solids and Structures*, *29*(19), 2355-2367.

Karim, M. R., Kundu, T., 1988. Transient surface response of layered isotropic and anisotropic half-spaces with interface cracks: SH case. *International Journal of Fracture*, 37, 245-262.

Karim, M. R., Kundu, T., Desai, C. S., 1989. Detection of delamination cracks in layered fiber-reinforced composite plates. *Journal of Pressure Vessel Technology*, 3,165-171.

Karunasena, W. M., Liew, K. M., Kitipornchai, S., 1995. Hybrid analysis of Lamb wave reflection by a crack at the fixed edge of a composite plate. *Computer methods in applied mechanics and engineering*, *125*(1-4), 221-233.

Loveday, P. W., Long, C. S., 2007. Time domain simulation of piezoelectric excitation of guided waves in rails using waveguide finite elements. *Sensors and Smart Structures Technologies for Civil, Mechanical, and Aerospace Systems*, 6529, 65290.

Mal, A., Chang, Z., 2000. A semi-numerical method for elastic wave scattering calculations. *Geophysical Journal International*, *143*(2), 328-334.

Marzani, A., Viola, E., Bartoli, I., Lanza di Scalea, F., Rizzo, P., 2008. A Semi-analytical Finite Element Formulation for modeling stress wave propagation in axisymmetric damped waveguides. *Journal of Sound and Vibration*, 318(3), 488-505.

Matt, H., Bartoli, I., Lanza di Scalea, F., 2005. Ultrasonic guided wave monitoring of composite wing skin-to-spar bonded joints in aerospace structures. *Journal of the Acoustical Society of America,* 118(4), 2240-2252.

Poddar, B. and Giurgiutiu, V., 2016a. Complex modes expansion with vector projection using power flow to simulate Lamb waves scattering from horizontal cracks and disbonds. *The Journal of the Acoustical Society of America,* 140(3), 2123-2133.

Poddar, B. and Giurgiutiu, V., 2016b. Scattering of Lamb waves from a discontinuity: an improved analytical approach. *Wave Motion*, 65, 79-91.

Rattanawangcharoen, N., Zhuang, W., Shah, A. H., Datta, S. K., 1997. Axisymmetric guided waves in jointed laminated cylinders. *ASCE Journal of Engineering Mechanics*, *123*(10), 1020-1026.

Rose, J. L., 2014. *Ultrasonic guided waves in solid media*. Cambridge university press.

Srivastava, A. and Lanza di Scalea, F., 2010. Quantitative structural health monitoring by ultrasonic guided waves. *ASCE Journal of Engineering Mechanics*, *136*(8), 937-944.

Staszewski, W., Boller, C., Tomlinson, G. R., 2004. *Health monitoring of aerospace structures: smart sensor technologies and signal processing*. John Wiley & Sons.

Tian, J., Gabbert, U., Berger, H., Su, X., 2004. Lamb wave interaction with delaminations in CFRP laminates. *Computers Materials & Continua*, *1*(4), 327-336.

Zhou, W. J., Ichchou, M. N., 2011. Wave scattering by local defect in structural waveguide through wave finite element method. *Structural Health Monitoring*, *10*(4), 335-349.